

Electronic supplementary materials *Mendeleev Commun.*, 2021, **31**, 784–788

Novel organic magnet derived from pyrazine-fused furazans

Victor I. Ovcharenko, Aleksei B. Sheremetev, Kirill V. Strizhenko, Sergey V. Fokin, Galina V. Romanenko, Artem S. Bogomyakov, Vitaly A. Morozov, Mikhail A. Syroeshkin, Anna Y. Kozmenkova, Andrey V. Lalov and Mikhail P. Egorov



Oxidation of H_2L with Br_2 vapor in an alkaline medium. Unlike the colorless H_2L solution, the L^\bullet - and $L^{\bullet\bullet}$ solutions are brightly colored green and dark brown, respectively. This makes it easy to register their appearance in the reaction mixture visually. The video shows how, when gaseous Br_2 is supplied into a flask with an alkaline aqueous solution of H_2L , L^\bullet - first accumulates at the interface, coloring the reaction mixture green, and then $L^{\bullet\bullet}$ appears on the surface, which causes a dark brown coloration of the solution surface.

[Click on image to play a movie](#)

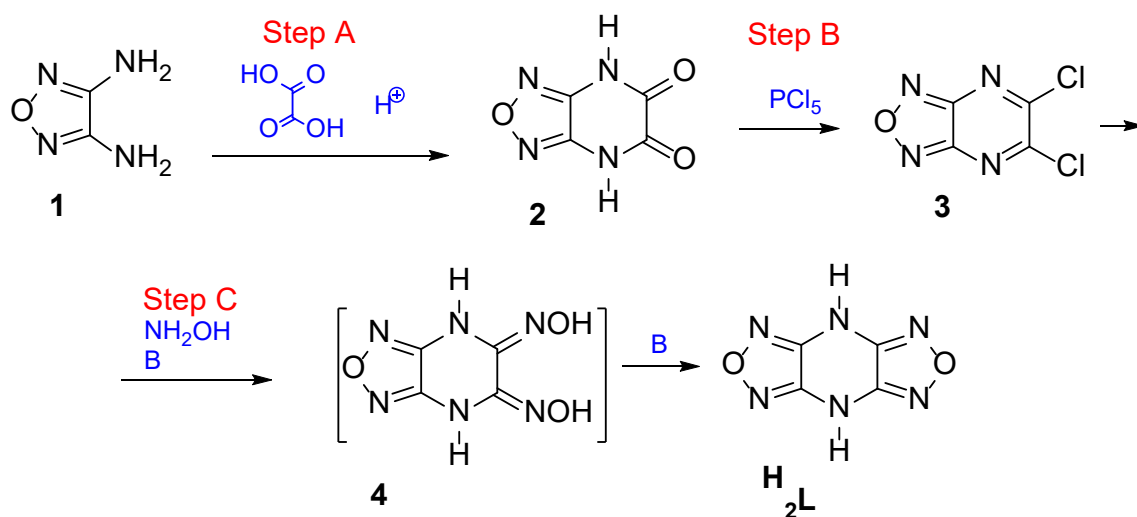
Contents:

1. Synthesis.....	S2
2. Electrochemical measurements	S7
2.1. Experiment.....	S7
2.2. Results.....	S7
3. Crystal structures	S14
3.1. Single crystal XRD experiments.....	S14
3.2. Crystal structures	S17
4. Magnetic properties	S24
5. Simultaneous electrochemical and electron spin resonance experiments and DFT calculation of HFC constants	S24
6. Calculations	S25
References	S26

1. Synthesis

Caution: Although none of the compounds described here has exploded or detonated in the course of this research, these materials should be handled with care using the best safety practices. Manipulations must be carried out in a hood behind a safety shield. Face shield and leather gloves must be worn. Caution should be exercised at all times during the synthesis, characterization, and handling of any of these materials.

Using the modified literature strategy^[1] outlined in Scheme S1, 4*H*,8*H*-bis(furazano)[3,4-*b*:3',4'-*e*]pyrazine (H₂L) was prepared from 3,4-diaminofurazan (**1**) in a total yield of *ca.* 27%. H₂L is slightly soluble in organic solvents, ethanol, and water and sparingly soluble in DMF. It is conveniently obtained by heating its saturated solution in DMF, which is allowed to stay for a week under normal conditions. The resulting perfect colorless crystals of H₂L·2DMF are suitable for an XRD study.



Scheme S1. Synthesis of 4*H*,8*H*-bis(furazano)[3,4-*b*:3',4'-*e*]pyrazine (H₂L)

The ring closure reaction of compound **1** with oxalic acid was accomplished in H₃PO₄ as an acid catalyst and solvent to give furazano[3,4-*b*]pyrazine-5,6(4*H*,7*H*)-dione (**2**) in 75% yield. In comparison, the previous synthetic method of **2** used highly corrosive hydrochloric acid as a solvent.^[2] In step B, 5,6-dichlorofurazano[3,4-*b*]pyrazine (**3**) was synthesized from compound **2** based on literature report.^[3] A two-step method for the preparation of H₂L from **3**, with the preparation and isolation of intermediate **4**, was described earlier^[4]. In our scheme, step C is implemented as a one-pot process, providing a direct conversion of compound **3** to H₂L. The following data illustrate modified reactions.

Furazano[3,4-b]pyrazine-5,6(4*H*,7*H*)-dione (2). A mixture of compound **1** (1 g, 10 mmol), oxalic acid (1.38 g, 15.4 mol) and of a 10% solution of orthophosphoric acid (1.5 ml) was heated under reflux for 3 h. After cooling the reaction mixture to room temperature, a precipitate was filtered off and dried overnight in air, and then in a desiccator at ~100°C until constant weight within (up to 3 h) to afford **2** as a white solid; yield: 1.154 g (75%); mp 294-295°C [mp 306-310 °C (dec.)]^[S2]. ¹H NMR (300.13 MHz, DMSO-*d*₆) δ 12.84 (bs, 2H). ¹³C NMR (75.47 MHz, DMSO-*d*₆) δ 144.7, 154.3. IR (KBr): ν 3284, 3126, 1715, 1598, 1352, 1015, 909, 845, 740, 676 cm⁻¹. Analysis calcd. for C₄H₂N₄O₃: C, 31.18; H, 1.31; N, 36.36. Found: C, 31.22; H, 1.33; N, 36.30.

5,6-Dichlorofurazano[3,4-b]pyrazine (3) was synthesized in accordance with the literature procedure.^[3] Mp 177–178°C [mp 170–175°C]^[3]. ¹³C NMR (75.47 MHz, CDCl₃) δ 150.2, 154.2. IR (KBr): ν 1573, 1531, 1462, 1402, 1296, 1158, 1032, 870, 819, 606, 465 cm⁻¹. Analysis calcd. for C₄Cl₂N₄O: C, 25.16; N, 29.34. Found: C, 25.23; N, 29.31.

4*H*,8*H*-Bis(furazano)[3,4-b:3',4'-e]pyrazine (H₂L). To a solution of NH₂OH×HCl (1.0 g, 144 mmol) in MeOH (8 mL) was added a solution of KOH (0.75 g, 134 mmol) in MeOH (3.5 mL) at room temperature. After the mixture was cooled to 0°C, compound **3** (0.5 g, 26 mmol) was slowly added and the resulting mixture stirred for 20 min. The reaction was then allowed to warm to room temperature, and hydrochloric acid was used to adjust the solution to pH 3. After 30 min, a mixture of intermediate **4** and inorganic salts (~1.4 g) was filtered off. The mixture was added to a solution of NaOH (1.05 g, 262 mmol) in water (3.5 mL) at room temperature to form a slurry. The reaction mixture was heated to 110°C for 6 h, cooled, and diluted with ethanol (2.5 mL). A solid was filtered off and washed with EtOH (1 mL) and ether (1 mL). The residue was dissolved in distilled H₂O (2.5 mL), and hydrochloric acid was used to adjust the solution to pH 1. The white precipitate was filtered and redissolved in ether. The organic layer was separated, the residue was then recrystallized from H₂O-*i*PrOH (1:1, 2 mL) to give H₂L (0.23 g, 53%): mp 292–293°C dec. [mp 294 °C]^[4]. ¹H NMR (300.13 MHz, DMSO-*d*₆) δ 11.82 (bs, 2H). ¹³C NMR (75.47 MHz, DMSO-*d*₆) δ 146.8. IR (KBr): ν 3276, 1653, 1593, 1442, 1327, 1077, 1001, 884, 825, 804 cm⁻¹. Analysis calcd. for C₄H₂N₄O₂: C, 28.92; H, 1.21; N, 50.60. Found: C, 28.90; H, 1.24; N, 50.55. H₂L is slightly soluble in organic solvents, ethanol, and water and sparingly soluble in DMF. It is conveniently obtained by heating its saturated solution in DMF, which is allowed to stay for a week under normal conditions. The resulting perfect colorless crystals of H₂L·2DMF are suitable for an XRD study.

H₂L·2DMF. The H₂L crystals (0.1 g) were dissolved in DMF (5 ml) while heating to 50–60°C. The colorless solution was cooled to room temperature and allowed to stay for 12 h at -18°C. The

resulting colorless needle crystals were separated by filtration, washed with ice water, and dried in air. This gave $\text{H}_2\text{L}\cdot 2\text{DMF}$ (0.7 g). Calculated for the partially desolvated product $\text{C}_4\text{H}_2\text{N}_6\text{O}_2\cdot 2\text{DMF}$ ($\text{C}_{10}\text{H}_{16}\text{N}_8\text{O}_4$), %: C, 38.5; H, 5.2. Found, %: C, 38.3; H, 5.9. A sample from one of the batches of $\text{H}_2\text{L}\cdot 2\text{DMF}$ crystals in a Petri dish is shown in Figure S1.



Figure S1. $\text{H}_2\text{L}\cdot 2\text{DMF}$ crystals.

H_2L was oxidized by two methods: stirring with PbO_2 and stirring with Br_2 vapor in an alkaline medium. In contrast to the colorless H_2L solutions, the solutions of $\text{L}^{\cdot -}$ and $\text{L}^{\cdot \cdot}$ are colored bright green and brown, respectively, due to which they are easily visualized in the reaction medium. The video in SI shows how the aqueous alkaline solution of H_2L changes after the feeding of Br_2 gas in the flask: at first $\text{L}^{\cdot -}$ accumulates at the interface, and the reaction mixture becomes green, and then bis(1,2,5-oxadiazolo)[3,4-*b*:3',4'-*e*]pyrazine ($\text{L}^{\cdot \cdot}$) appears on the surface of the solution, due to which the latter is colored brown (SI, Video).

$\text{L}^{\cdot \cdot}$. A mixture of H_2L (0.0500 g, 0.3 mmol) and LiOH (0.0144 g, 0.6 mmol) (any alkali hydroxide can be used) was dissolved, while heating, in H_2O (7 ml), and the solution was cooled to room temperature. The resulting colorless solution was kept in a chamber (8000 cm^3) with bromine vapor, which spontaneously evaporated from the open glass. The reaction mixture gradually became at first green and then wine-colored. After 1 h, crystal aggregates of $\text{L}^{\cdot \cdot}$ started to form. After 3 h, the dark wine-colored crystals with metallic luster were separated by filtration, washed with ice water, and dried in air. Yield 21%. Calculated for $\text{C}_4\text{N}_6\text{O}_2$, %: C, 29.3; N, 51.2. Found, %: C, 28.9; N, 51.3. A batch of crystal aggregates of $\text{L}^{\cdot \cdot}$ under a microscope is shown in Figure S2.

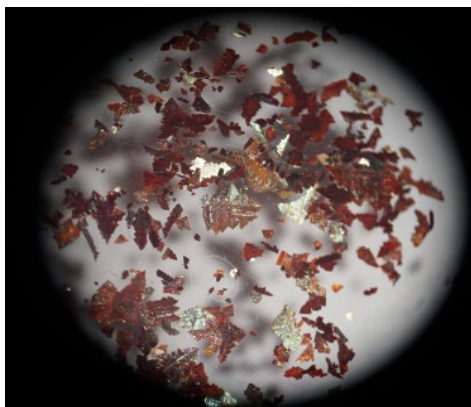


Figure S2. Crystal aggregates of L'' under a microscope.

$NH_4(L^+)(H_2O)$. H_2L (0.0500 g, 0.3 mmol) was dissolved in a concentrated ammonia solution (~25%, 7 ml); then PbO_2 (0.5 g) was added, and the mixture was stirred for 3 h. The dark green solution was filtered and allowed to stay for 12 h at 6°C. The resulting black green needle crystals were separated by filtration, washed with ice water, and dried in air. Yield 32%. Calculated for $C_4H_6N_7O_3$, %: C, 24.0; H, 3.0; N, 49.0. Found, %: C, 23.4; H, 3.1; N, 49.2.

$Li(L^+)(H_2O)_3$. A mixture of H_2L (0.0500 g, 0.3 mmol) and $LiOH$ (0.0288 g, 1.2 mmol) was dissolved, while heating, in H_2O (5 ml) in a conical 10-ml flask, and the solution was cooled to room temperature. The resulting colorless solution was kept in a chamber (600 cm³) with Br_2 vapor with stirring (note that PbO_2 does not oxidize H_2L in the presence of $LiOH$). The reaction mixture gradually became green-colored. After 30 min, the dark green solution was taken out of the chamber and allowed to stay for 20 h at 6°C. More prolonged interaction with Br_2 vapor leads to the formation of an L'' impurity, which can be eliminated by adding more $LiOH$ to the solution. The resulting black green needle crystals were separated by filtration, washed with ice water, and dried in air. Yield 38%. Calculated for $C_4H_6LiN_6O_5$, %: C, 21.4; H, 2.7; N, 37.3. Found, %: C, 21.8; H, 2.4; N, 37.6. The substance is soluble in MeCN and acetone.

$Na(L^+)(H_2O)_3$. A mixture of H_2L (0.1000 g, 0.6 mmol) and $NaOH$ (0.0482 g, 1.2 mmol) was dissolved, while heating, in H_2O (5 ml), and the solution was cooled to room temperature. PbO_2 (0.5 g) was added to the resulting colorless solution, and the mixture was stirred for 3 h. The dark green solution was filtered and allowed to stay for 18 h at 6°C. The resulting precipitate of black green needle crystals (Figure S3) were separated by filtration, washed with ice water, and dried in air. Yield 48%. Calculated for $C_4H_6N_6NaO_5$, %: C, 19.9; H, 2.5; N, 34.9. Found, %: C, 19.7; H, 2.8; N, 35.1. **$K(L^+)(H_2O)_{2.5}$** and **$Rb(L^+)(H_2O)$** were obtained by a similar procedure. The yield of **$K(L^+)(H_2O)_{4.5}$** was 52%. Calculated for the partially dehydrated product **$K(L^+)\cdot 5/3H_2O$** – $C_{12}H_{10}K_3N_{18}O_{11}$, %: C, 20.6; H, 1.4; N, 36.0. Found, %: C, 20.2; H, 1.2; N, 36.2. The yield of **$Rb(L^+)(H_2O)$** was 43%. Calculated for $C_8H_4N_{12}O_6Rb_2$, %: C, 18.0; H, 0.8; N, 31.4. Found, %: C, 17.6; H, 1.1; N, 31.6.

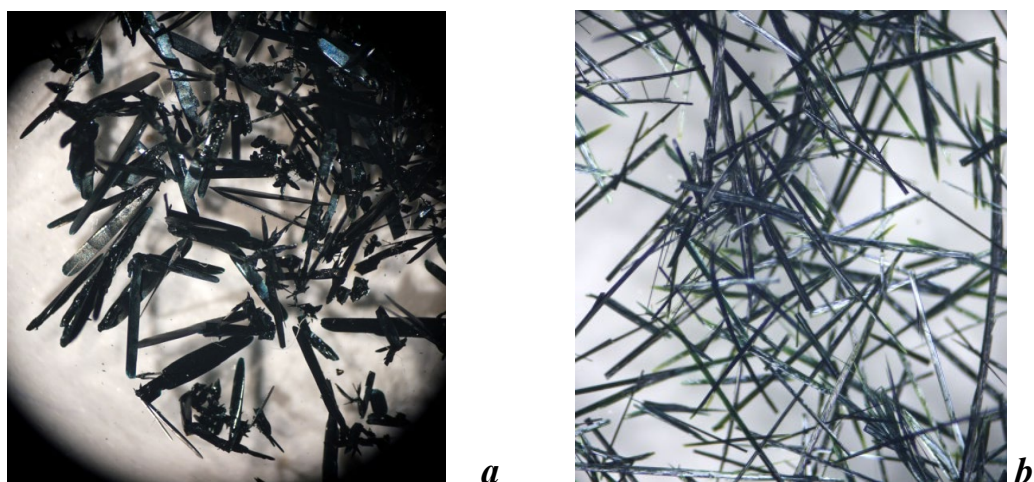


Figure S3. $\text{Na}(\text{L}^*)(\text{H}_2\text{O})_3$ crystals under a microscope (a); thin $\text{Na}(\text{L}^*)(\text{H}_2\text{O})_3$ whiskers did not decompose after a year of storage in the fridge (b).

2. Electrochemical measurements

2.1. Experiment

The electrochemical parameters of the oxidation and reduction of H₂L were determined by cyclic voltammetry using a three-electrode glass cell with two additional holes for gas inlet and outlet during the cell purging. The working electrode was a polished glassy carbon disc electrode with a disk diameter of 1.7 mm. The working surface of the electrode was polished to a mirror shine with sandpaper and GOI paste before use. The auxiliary electrode was a platinum wire preliminarily annealed on a gas burner to remove oxides and other impurities. The process potentials were measured relative to a saturated silver chloride reference electrode ($E^0 = 0.222$ V) separated from a bulk electrolyte by an electrode junction. The compound H₂L was dissolved in a supporting electrolyte, which was a 0.1 M solution of Bu₄NBF₄ in MeCN. The concentration of H₂L was $3 \cdot 10^{-3}$ M. Before the measurements, the electrolyte was purged with high-purity argon through a capillary submerged in the solution for 10 min to remove dissolved oxygen. The cyclic voltammetry measurements were performed at a potential scan rate of 100 mV/s at potentials in the potential range $-2.8 - 2.8$ V relative to Ag/AgCl; in the case of reversible or quasi-reversible processes, the scan rates of 50 and 400 mV/s were also used for determining the half-wave potential. In addition, H₂L was dissolved in a supporting electrolyte—a 0.1 M LiClO₄ solution in water. In this case, the cyclic voltammetry (CV) measurements were performed at a potential scan rate of 100 mV/s in the potential range $-1.8 - 1.8$ V relative to Ag/AgCl; in the case of reversible or quasi-reversible processes, the scan rates of 50, 200, 500, and 1000 mV/s were also used for determining the half-wave potential. All measurements were carried out using an IPC-Pro MF potentiostat.

2.2. Results

The oxidation curve of H₂L (Figure S4) contains two peaks. The main peak ($E_p = 1.49$ V) corresponds to the oxidation of the starting pyrazine-fused furazan; and the second peak in the range of lower potentials ($E_p = 0.93$ V), to the oxidation of its monodeprotonated form HL[−], which appears during the partial dissociation of H₂L—a rather strong Brønsted acid.

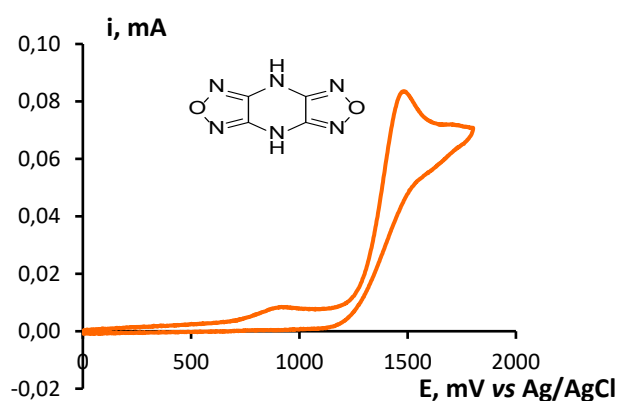


Figure S4. CV curve of oxidation obtained for the $3 \cdot 10^{-3}$ M H_2L solution in 0.1 M $\text{Bu}_4\text{NBF}_4/\text{MeCN}$ at a potential scan rate of 100 mV/s on a glassy carbon disc electrode.

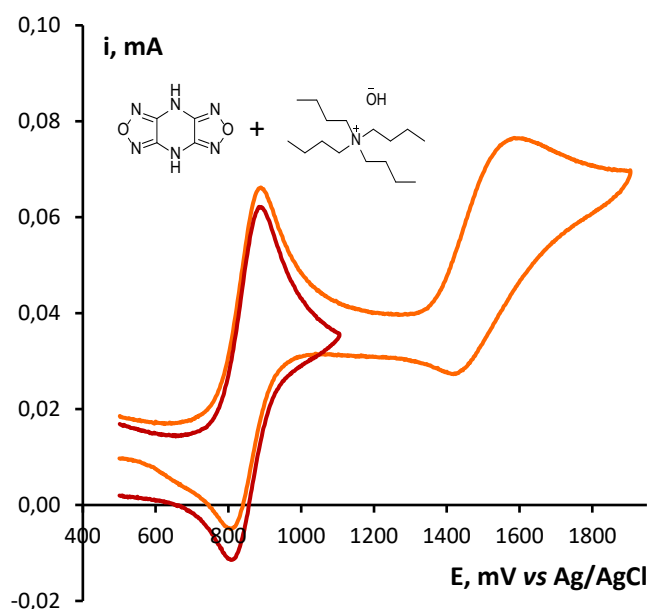


Figure S5. CV curves obtained on a glassy carbon disc electrode for the $3 \cdot 10^{-3}$ M H_2L solution in 0.1 M $\text{Bu}_4\text{NBF}_4/\text{MeCN}$ after the addition of an equimolar amount of Bu_4NOH . The potential scan rate is 100 mV/s.

Indeed, after the addition of an equimolar amount of Bu_4NOH to the solution, this peak drastically increased (and slightly shifted toward the cathode side to $E_p = 0.87$ V), and the peak corresponding to the oxidation of the starting H_2L decreased proportionally (Figure S5). Also note that after the addition of the base, the oxidation of H_2L remained almost irreversible (Figure S5, second peak), while for the oxidation of HL^- , the shape of the CV curve became similar to the shape characteristic for reversible processes (Figure S5, first peak). The CV curves obtained at different potential scan rates in the range that covers the oxidation of HL^- alone were analyzed by constructing the dependences of the potentials of the oxidation and reduction peaks on the peak

current (Figure S6). Approximation of these dependences to zero current allowed us to determine the potentials of the oxidation peak and response reduction peak without the uncompensated resistance effect, and also the half-wave potential (Table S1).

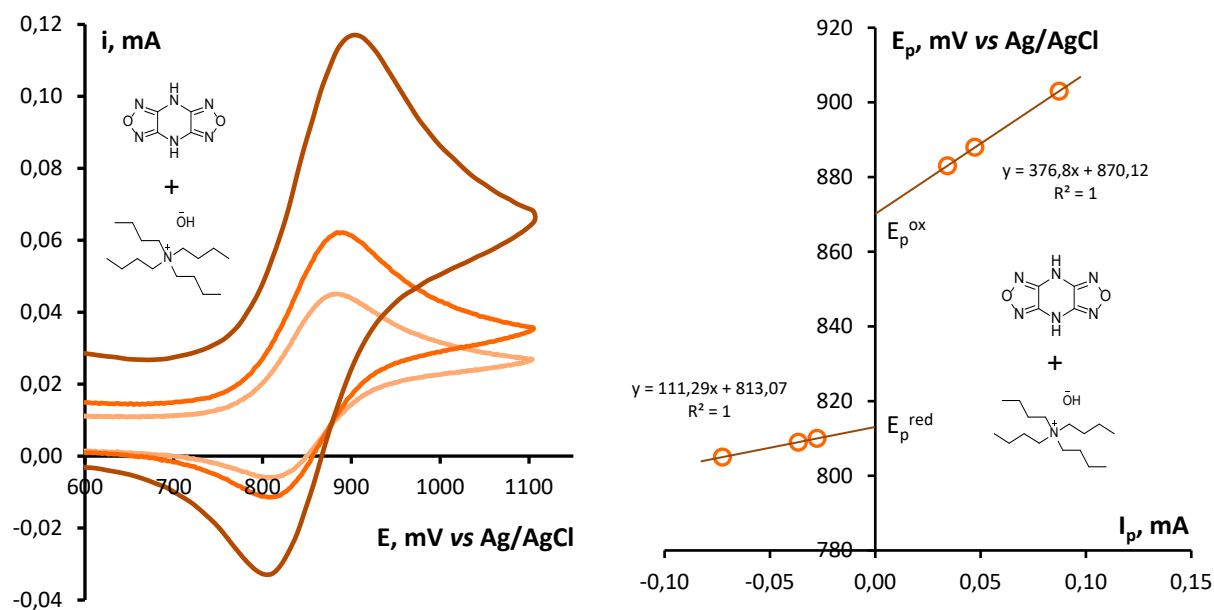


Figure S6. CV curves obtained on a glassy carbon disc electrode for the $3 \cdot 10^{-3}$ M H_2L solution in 0.1 M $Bu_4NBF_4/MeCN$ after the addition of an equimolar amount of Bu_4NOH . The potential scan rates are 50, 100, and 400 mV/s (*left*). Dependences of the oxidation and reduction peak potentials on the peak current for the indicated curves (*right*).

Table S1. Electrochemical characteristics obtained by treatment of the voltammetric curves shown in Figure S6.

E_p^{red} , mV	E_p^{ox} , mV	$E_{1/2}$, mV	ΔE , mV
813	870	842	57

After the addition of one more equivalent of Bu_4NOH , the oxidation peak of the starting H_2L vanished, while that of HL^- remained ($E_p = 0.89$ V) (Figure S7). At the same time, new peaks appeared at -0.31 V and 0.20 V; the former relates to the oxidation of L^{2-} , whose concentration significantly increased after the addition of another equivalent of base, and the latter is due to the oxidation of $L^{\cdot-}$ that formed during the first process. The oxidation of both HL^- and L^{2-} proved almost completely reversible. The CV curves for these processes obtained at different potential scan rates and the results of their analysis are shown in Figures S8 and S9, respectively; the oxidation, reduction, and half-wave potentials are presented in Table S2. All these processes for H_2L are summarized in Scheme 3.

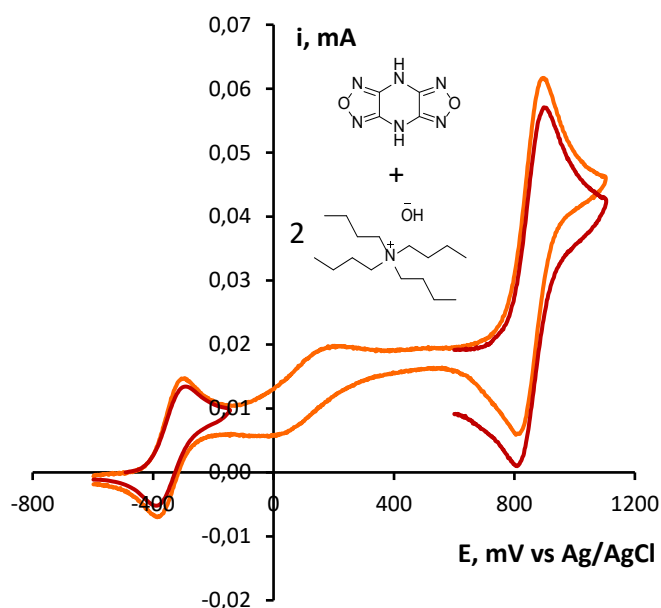


Figure S7. CV curves obtained on a glassy carbon disc electrode for the $3 \cdot 10^{-3}$ M H_2L solution in 0.1 M $Bu_4NBF_4/MeCN$ after the addition of Bu_4NOH in an amount that is two times the content of H_2L . The potential scan rate is 100 mV/s.

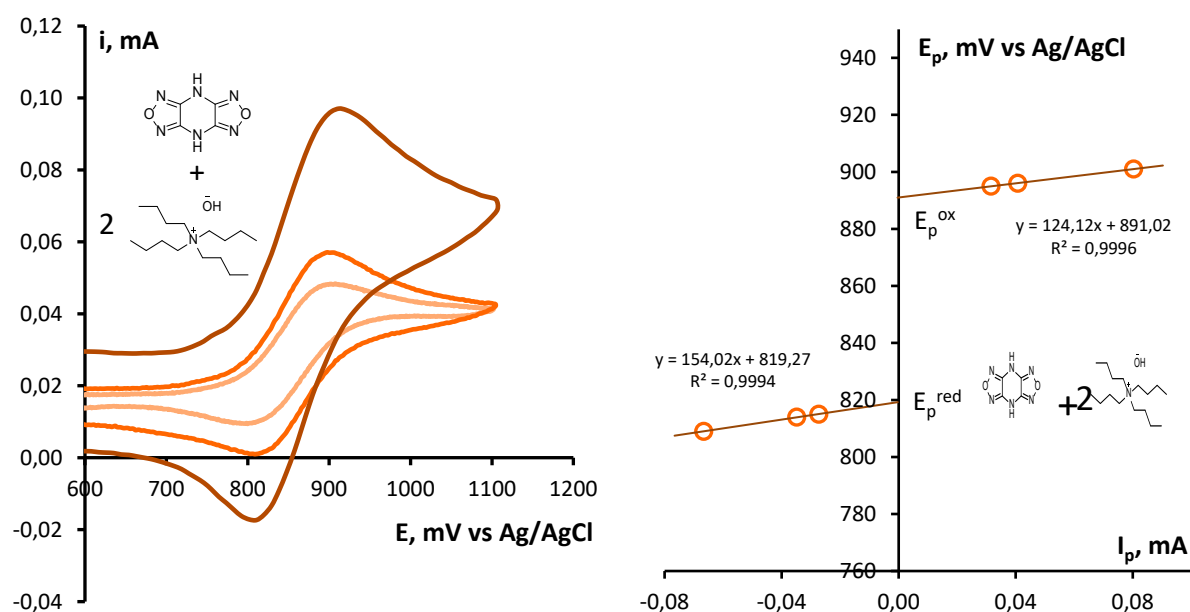


Figure S8. CV curves obtained on a glassy carbon disc electrode for the $3 \cdot 10^{-3}$ M H_2L solution in 0.1 M $Bu_4NBF_4/MeCN$ after the addition of Bu_4NOH in an amount that is two times the content of H_2L . The region of oxidation of HL^- at potential scan rates of 50, 100, and 400 mV/s is shown (*left*). Dependences of the oxidation and reduction peak potentials on the peak current for the indicated curves (*right*).

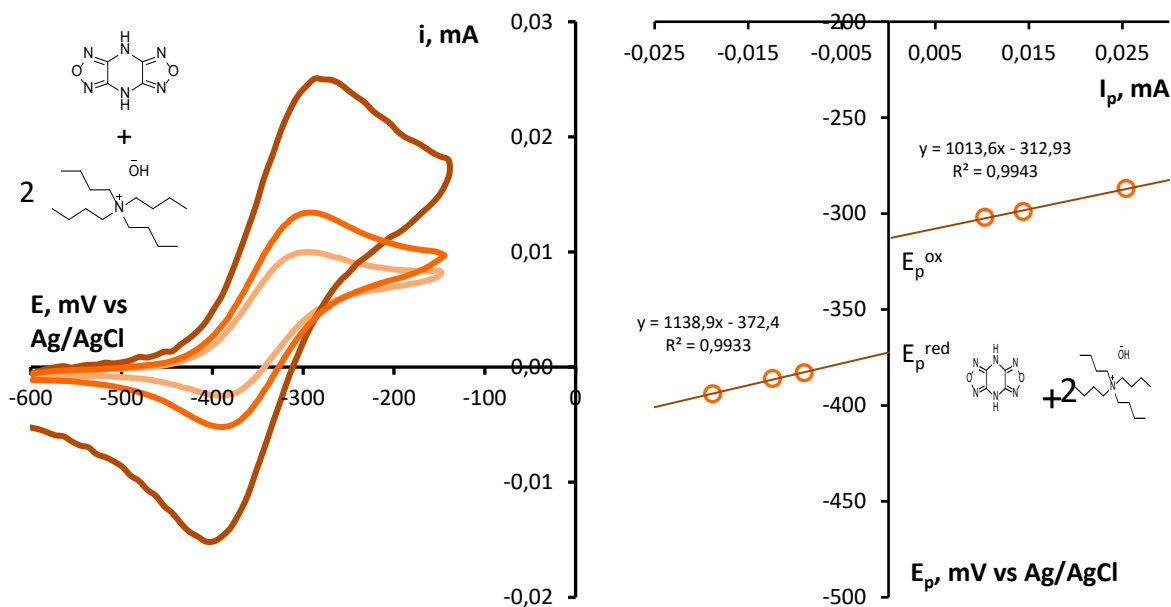


Figure S9. CV curves obtained on a glassy carbon disc electrode for the $3 \cdot 10^{-3}$ M H_2L solution in 0.1 M $Bu_4NBF_4/MeCN$ after the addition of Bu_4NOH in an amount that is two times the content of H_2L . The region of oxidation of L^{2-} at potential scan rates of 50, 100, and 400 mV/s is shown (*left*). Dependences of the oxidation and reduction peak potentials on the peak current for the indicated curves (*right*).

Table S2. Electrochemical characteristics obtained by processing the voltammetric curves shown in Figures S8 and S9.

E_p^{red} , mV	E_p^{ox} , mV	$E_{1/2}$, mV	ΔE , mV
-372	-313	-343	59
819	891	855	72

The reduction peak of H_2L shifted to the region of negative potentials after the addition of the base to the solution. The electrochemical parameters are given in Table S3.

Table S3. Reduction (E_p^{red}), oxidation (E_p^{ox}), and half-wave ($E_{1/2}$) peak potentials for the reversible (quasi-reversible) oxidation in 0.1 M $Bu_4NBF_4/MeCN$ obtained by cyclic voltammetry on a glassy carbon disc electrode ($d = 1.7$ mm) at 298 K.

Solution	Potential, mV, relative to Ag/AgCl		
	E_p^{red}	E_p^{ox}	$E_{1/2}$
H_2L	-2224	934 1489	
$H_2L + Bu_4NOH$	-2720	870 1472	842
$H_2L + 2Bu_4NOH$	-2720	-308 203 890	-343 855

The electrochemical parameters of oxidation and reduction of H₂L were also determined in a supporting electrolyte based on water. According to Figure S10, at a positive potential scan, the voltammetric curve has a peak at $E_p = 0.84$ V corresponding to the oxidation of HL⁻ to the radical and a response reduction peak, which agrees with the data obtained in acetonitrile. In contrast to the experiment in acetonitrile, in aqueous media this process occurs without base additions (Bu₄NOH), which corresponds to a strengthening of acid properties of H₂L on passing from acetonitrile to water. The shape of the CV curve is similar to that characteristic for the reversible processes. The CV curves recorded at different potential scan rates in the range that corresponds only to the process under study were analyzed by constructing the dependences of the oxidation and reduction peak potentials on the peak current (Figure S11). Approximation of these dependences to zero current allowed us to determine the oxidation and response reduction potentials without the uncompensated resistance effect, and also the half-wave potential (Table S4).

The reduction curve did not reflect any processes until the discharge of the supporting electrolyte took place.

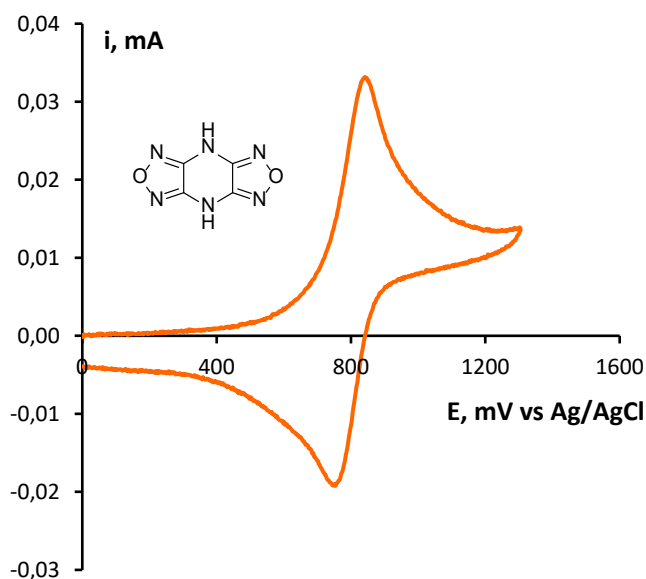


Figure S10. CV curves obtained for the $3 \cdot 10^{-3}$ M H₂L solution in 0.1 M LiClO₄/H₂O at a potential scan rate of 100 mV/s on a glassy carbon disc electrode.

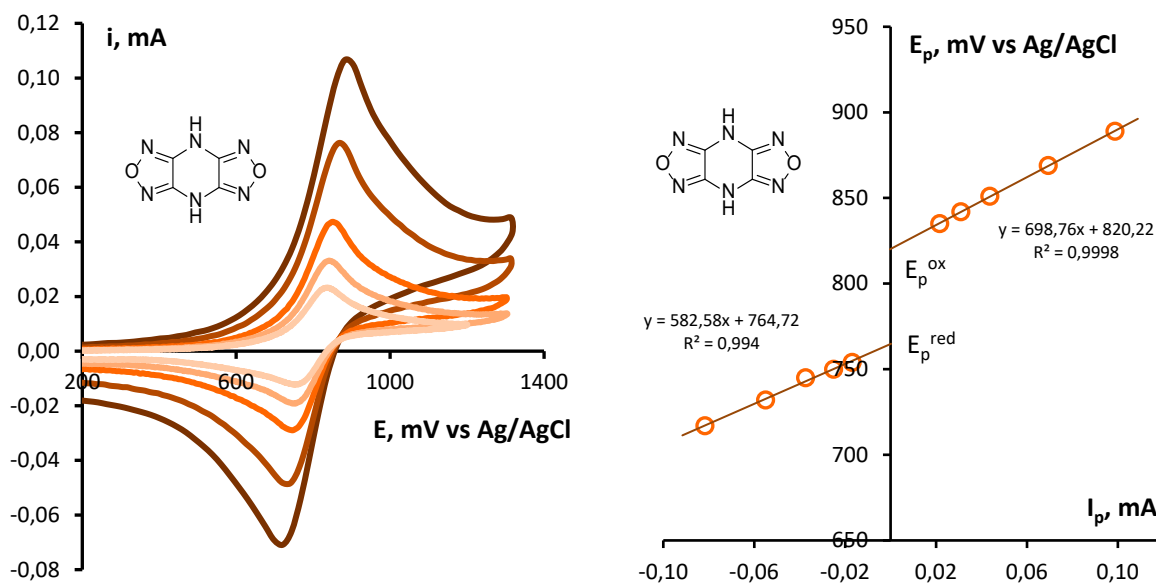


Figure S11. CV curves obtained on a glassy carbon disc electrode for the $3 \cdot 10^{-3}$ M H_2L solution in 0.1 M $LiClO_4/H_2O$ at potential scan rates of 50, 100, 200, 500, and 1000 mV/s (*left*). Dependences of the oxidation and reduction potentials on the peak current for the indicated curves (*right*).

Table S4. Electrochemical characteristics obtained by processing the voltammetric curves shown in Figure S11.

E_p^{red} , mV	E_p^{ox} , mV	$E_{1/2}$, mV	ΔE , mV
765	820	793	55

3. Crystal structures

3.1. Single crystal XRD experiments

The crystals suitable for an XRD analysis were mostly collected directly from the mother solution and immersed into epoxide resin for protection from medium effects. Data sets were obtained on Bruker AXS – SMART APEX II and Apex Duo diffractometers (absorption correction and scaling was done using SADABS program, ver. 2.10). The structures were solved by direct methods and refined by full-matrix least squares anisotropically for all non-hydrogen atoms. For the majority of structures, the positions of H atoms were located in series of electron density syntheses and refined in an isotropic approximation without any restrictions. In some cases, they were calculated geometrically and refined in a riding model with free thermal parameters. All calculations on structure solution and refinement were performed with the Bruker SHELXTL (ver. 6.14) and SHELX set of programs^[5]. The crystal data for the compounds, details of experiments and CCDC deposition numbers are given in Tables S5 and S6. These data can be obtained free of charge via <http://www.ccdc.cam.ac.uk/cgi-bin/catreq.cgi>, or from the Cambridge Crystallographic Data Centre, 12 Union Road, Cambridge CB2 1EZ, UK; fax: (+44) 1223 336 033; or e-mail: deposit@ccdc.cam.ac.uk.

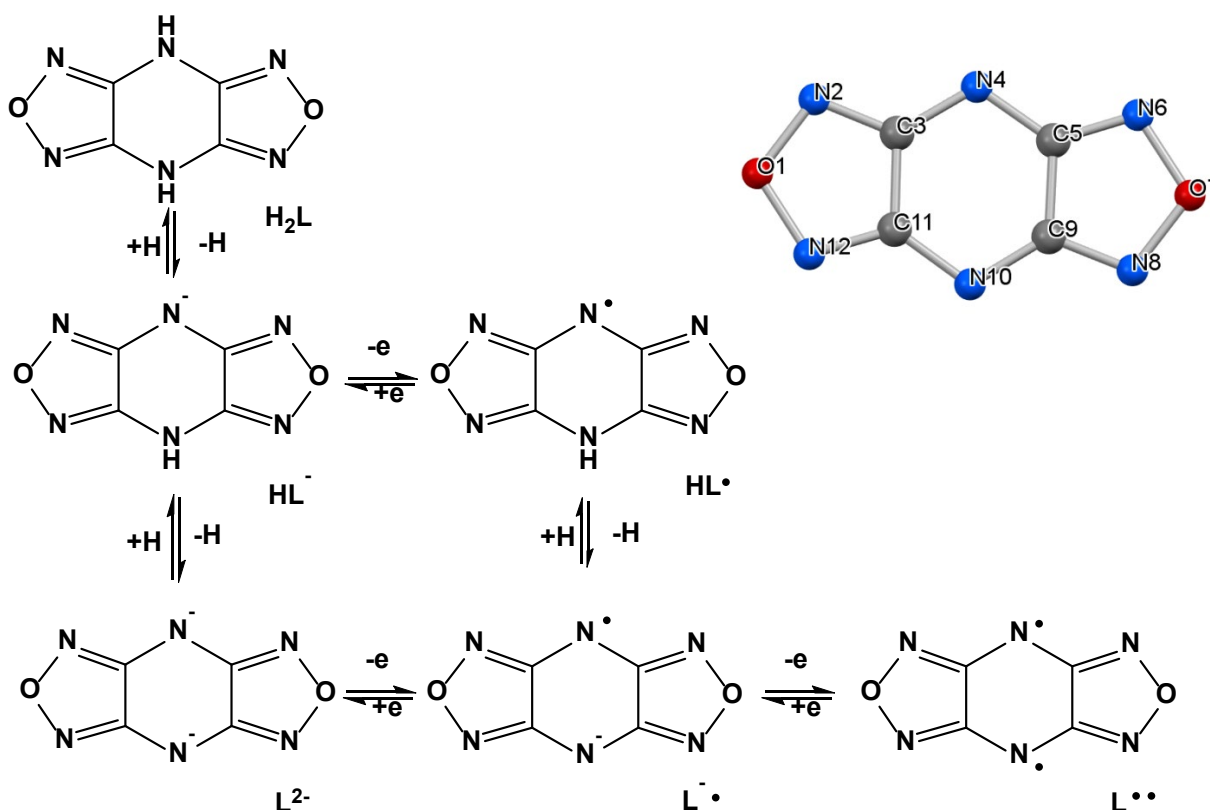
Table S5. Crystal data and details of XRD experiments

Compound	H ₂ L ^[7]	H ₂ L·2DMF	(NH ₄)(L ⁺)(H ₂ O) ₃	L ⁺
Formula	C ₄ H ₂ N ₆ O ₂	C ₁₀ H ₁₆ N ₈ O ₄	C ₄ H ₁₀ N ₇ O ₅	C ₄ N ₆ O ₂
FW	166.00	312.31	234.20	164.10
T, K	110	296	296	296
Space group, <i>Z</i>	<i>P</i> 2 ₁ / <i>n</i> , 2	<i>C</i> 2/ <i>c</i> , 4	<i>P</i> 2 ₁ / <i>c</i> , 4	<i>Cmca</i> , 4
<i>a</i> ,	5.1253(1)	21.1751(12)	8.6393(6)	15.935(4)
<i>b</i> ,	4.4839(1)	4.1239(2)	6.7123(5)	5.6876(14)
<i>c</i> , Å	11.8178(3)	18.4848(10)	8.8415(6)	6.6326(18)
β , °	91.072(1)	115.567(2)	103.154(5)	90
<i>V</i> , Å ³	271.54(1)	1456.11(14)	499.26(6)	601.1(3)
<i>D</i> _{calc} , g/cm ³	2.032	1.425	1.574	1.813
μ , mm ⁻¹	0.170	0.964	0.141	1.335
θ_{\max} , °	80.000	68.034	28.317	67.080
<i>I</i> _{hkl} total / uniq / <i>R</i> _{int}	6876 / 1645 / 0.0193	6039 / 1309 / 0.0221	8603 / 1236 / 0.1153	740 / 269 / 0.0505
<i>I</i> _{hkl} (<i>I</i> > 2 σ _{<i>I</i>}) / N	1494 / 59	1237 / 133	842 / 108	227 / 30
<i>Goof</i>	1.109	1.007	0.909	1.058
<i>R</i> 1 / <i>wR</i> 2 (<i>I</i> > 2 σ _{<i>I</i>})	0.0424	0.0344 / 0.1042	0.0353 / 0.0877	0.0484 / 0.1389
<i>R</i> 1 / <i>wR</i> 2 (all data)	0.0885	0.0358 / 0.1068	0.0531 / 0.0956	0.0538 / 0.1456
CCDC	RIRGAA01	2081749	2081752	2081747

Table S6. Crystal data and details of XRD experiments

Compound	Li(L ⁺)(H ₂ O) ₃	Na(L ⁺)(H ₂ O) ₃	K(L ⁺)(H ₂ O) _{2.5}	Rb(L ⁺)(H ₂ O)
Formula	C ₄ H ₆ LiN ₆ O ₅	C ₄ H ₆ N ₆ NaO ₅	C ₄ H ₅ KN ₆ O _{4.5}	C ₄ H ₂ N ₆ O ₃ Rb
FW	225.09	241.14	248.24	267.58
T, K	296	296	283	296
Space group, <i>Z</i>	<i>Cc</i> , 4	<i>P</i> -1, 2	<i>C2/c</i> , 8	<i>P</i> -1, 2
<i>a</i> ,	16.4101(5)	3.5452(5)	22.6136(10)	13.4013(5)
<i>b</i> ,	6.4572(2)	8.0940(9)	4.0120(2)	6.7965(3)
<i>c</i> , Å	8.6603(3)	16.206(2)	20.2128(9)	9.5489(3)
<i>α</i> , °		102.815(9)		69.178(2)
<i>β</i> , °	104.164(2)	94.891(10)	94.951(2)	85.648(2)
<i>γ</i> , °		90.540(9)		77.650(2)
<i>V</i> , Å ³	889.78(5)	451.60(10)	1826.98(15)	794.12(5)
<i>D</i> _{calc} , g/cm ³	1.680	1.773	1.805	2.238
<i>μ</i> , mm ⁻¹	1.316	1.799	0.597	6.227
<i>θ</i> _{max} , °	67.376	67.604	29.218	29.520
<i>I</i> _{hkl} total / uniq / <i>R</i> _{int}	3426 / 1408 / 0.0608	3631 / 1545 / 0.0301	9469 / 2482 / 0.0399	15031 / 4249 / 0.1006
<i>I</i> _{hkl} (<i>I</i> > 2σ _{<i>I</i>}) / N	1382 / 180	1225 / 170	1678 / 161	2951 / 270
<i>Goof</i>	1.054	1.120	0.965	0.844
<i>R</i> 1 / <i>wR</i> 2 (<i>I</i> > 2σ _{<i>I</i>})	0.0437 / 0.1077	0.0429 / 0.1226	0.0342 / 0.0768	0.0399 / 0.0808
<i>R</i> 1 / <i>wR</i> 2 (all data)	0.0453 / 0.1087	0.0542 / 0.1306	0.0558 / 0.0838	0.0646 / 0.0890
CCDC	2081753	2081748	2081750	2081751

3.2. Crystal structures



Scheme S2. Various oxidative states of 4*H*,8*H*-bis(1,2,5-ozadiazolo)[3,4-*b*:3',4'-*e*]pyrazine.

The literature contains data concerning the structure of the potassium salt of H_2L and $L^{\bullet\bullet}$.^[6] However, the potassium salt $K(L^{\bullet})(H_2O)_{2.5}$ described in the present article has another composition and absolutely different structure of the solid phase. As for $L^{\bullet\bullet}$, it was described in the literature as a product representing a mixture of the paramagnetic and diamagnetic forms. The compound $L^{\bullet\bullet}$ obtained by us also differs from the described product in its structure. In addition, it is diamagnetic over the entire range of measurements, which fully agrees with the data of quantum-chemical calculations. Recently, the results of a precision XRD study of H_2L at 110 K were published, in which the structure was determined and electron density distribution in crystals was examined;^[7] it was shown that electron density was delocalized over the central part of the molecule and did not extend to the O atoms. For convenient comparison of the available results and our structural data, the first two columns of Table S7 give the literature data.^[6,7]

We determined the crystal structure of the solvate $H_2L \cdot 2DMF$. In the structure of $H_2L \cdot 2DMF$, as well as in H_2L , the dihydrodifurazanopyrazine molecules are centrosymmetric and almost planar. The bond lengths in the furazan rings C–N_F (N2–C3 and N5–C6 1.2944(2)–1.3040(7) Å) are much shorter than those in the pyrazine ring (C3–N4 and N4–C5 1.3669(2)–1.3763(7) Å). The angles at the pyrazine N atoms (below, N_P) are 114.85(1)–114.89(4)° (Table S7).

In the structure of $\text{H}_2\text{L}\cdot 2\text{DMF}$, each H_2L molecule is linked with two DMF molecules (Figure S12) by hydrogen bonds between the $\text{N}_\text{p}\text{H}$ groups of the pyrazine ring and the O_DMF atoms ($\text{N4}\cdots\text{H4}$ 0.95(2), $\text{H4}\cdots\text{O1A}$ 1.74(2), $\text{N4}\cdots\text{O1A}$ 2.686(1) Å, $\text{N4}\text{--H4--O1A}$ 179(2)°). The H_2L molecules form stacks along the [010] direction, in which the short contacts are the intermolecular $\text{C}\cdots\text{C}$ distances equal to 3.299 Å.

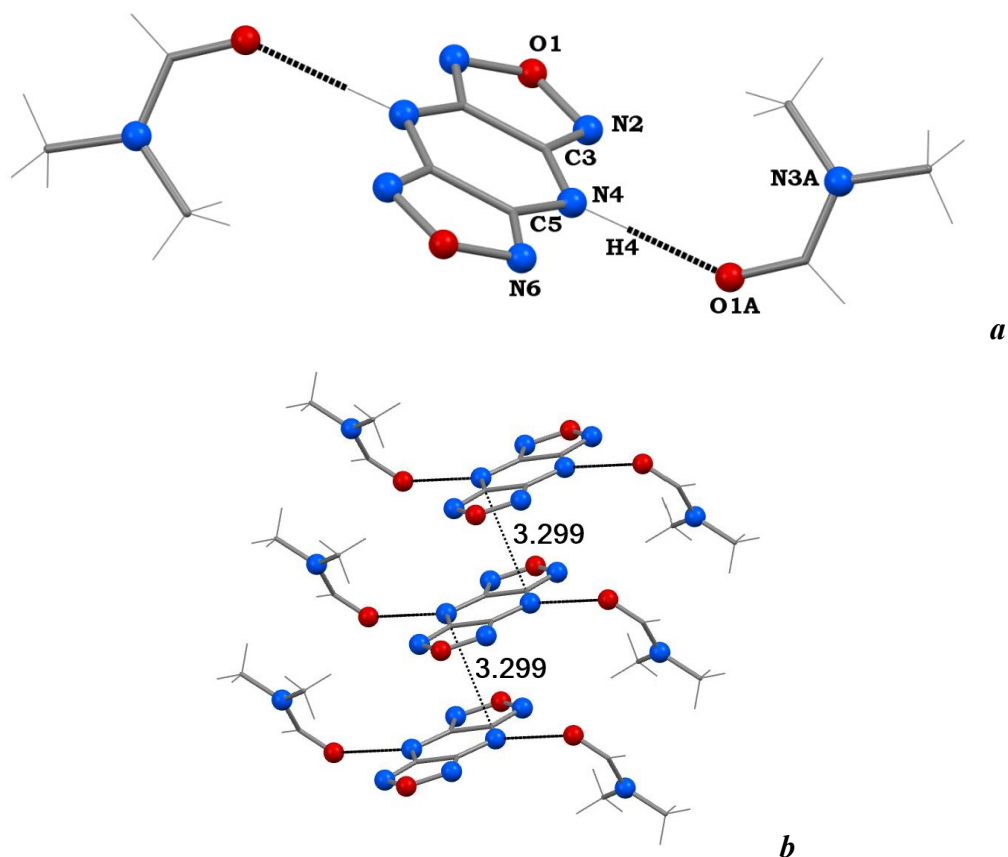


Figure S12. Fragments of structure (a) and molecular stacks (b) in $\text{H}_2\text{L}\cdot 2\text{DMF}$. Here and below, the dashed line shows the hydrogen bonds and short contacts in the structures.

In the planar, highly symmetric L^{**} molecule (D_{2h} symmetry), the C--N_F bond lengths in the furazan rings are longer by ~ 0.03 Å relative to those in H_2L (1.329(3) Å versus 1.2944(2) in $\text{H}_2\text{L}\cdot 2\text{DMF}$), while in the pyrazine ring, they are shorter by the same value (1.335(2) Å versus 1.3669(2) Å in $\text{H}_2\text{L}\cdot 2\text{DMF}$). The angles at the pyrazine N_p atoms are smaller by more than 5° ($108.8(2)$ and $114.85(1)^\circ$). The angle between the planes of adjacent molecules is 67.1° . The $\text{N}\cdots\text{C}$ short contacts between adjacent molecules (3.227 Å), which are smaller than the sum of the van der Waals radii of the atoms, allow us to conventionally identify layers (Figure S13) parallel to (100). The shortest interlayer distances are the $\text{O}_\text{F}\cdots\text{N}_\text{F}$ contacts of the furazan rings (3.239 Å).

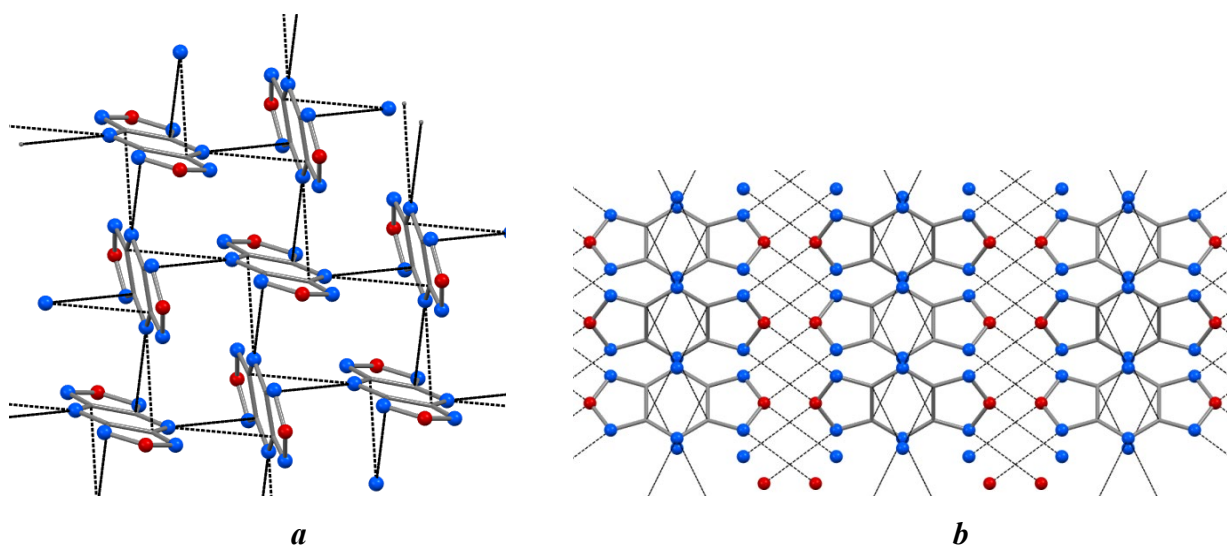


Figure S13. Fragment of layer in the structure of L'' (a) and the structure projected along the $[001]$ direction (b).

Table S7. Bond lengths and angles (\AA , deg) in $H_2L \cdot 2DMF$, $(NH_4)(L^*)(H_2O)_3$, and L'' . The atomic numbering scheme is given in Scheme S2.

Parameter	$L^{[6]}$	$H_2L^{[7]}$	$H_2L \cdot 2DMF$	$(NH_4)(L^*)(H_2O)_3$	L''
O1-N2	1.416	1.4029(6)	1.4069(2)	1.3843(15)	1.359(3)
N2-C3	1.227	1.3040(7)	1.2944(2)	1.3191(16)	1.329(3)
C3-N4	1.488	1.3730(6)	1.3669(2)	1.3497(15)	1.335(2)
N4-C5	1.417	1.3763(7)	1.3687(2)	1.3487(16)	1.335(2)
C5-N6	1.227	1.3014(7)	1.2946(2)	1.3201(18)	1.329(3)
N6-O7	1.395	1.3955(7)	1.4037(2)	1.3944(16)	1.359(3)
O7-N8	1.399	1.4029(6)	1.4069(2)	1.3843(15)	1.359(3)
N8-C9	1.391	1.3040(7)	1.2944(2)	1.3191(16)	1.329(3)
C9-N10	1.267	1.3730(6)	1.3669(2)	1.3497(15)	1.335(2)
N10-C11	1.312	1.3763(7)	1.3687(2)	1.3487(16)	1.335(2)
C11-N12	1.380	1.3014(7)	1.2946(2)	1.3201(18)	1.329(3)
N12-O1	1.427	1.3955(7)	1.4037(2)	1.3944(16)	1.359(3)
C3-C11	1.432	1.4425(7)	1.4314(2)	1.4482(19)	1.434(4)
C5-C9	1.486	1.4425(7)	1.4314(2)	1.4482(19)	1.434(4)
$\angle C3-N4-C5$	112.7	114.89(4)	114.85(1)	109.61(11)	108.8(2)
$\angle C9-N10-C11$	115.5	114.89(4)	114.85(1)	109.61(11)	108.8(2)

In the crystals of all compounds under study except L'' , the difurazanopyrazine molecules form stacks similar to those described for $H_2L \cdot 2DMF$ with intermolecular distances of 3.12–3.30 \AA .

A fragment of the structure of $(NH_4)(L^*)(H_2O)_3$ with disordered H_2O molecules and NH_4^+ cations is given in Figure S14. It shows that the columns of L^* anions are separated by the hydrogen-bonded H_2O molecules and NH_4^+ cations.

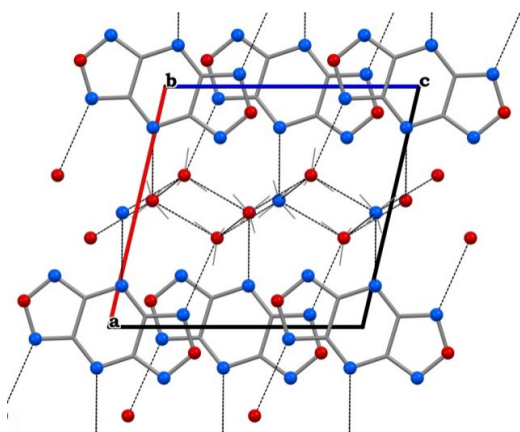


Figure S14. Structure of $(\text{NH}_4)(\text{L}^\bullet)(\text{H}_2\text{O})_3$ projected along the $[010]$ direction.

In the $\text{Li}(\text{L}^\bullet)(\text{H}_2\text{O})_3$ crystals, the Li atom lies in a tetrahedron formed by the N atom of one of the furazan rings ($\text{Li}-\text{N}$ 2.206(8) Å) and three OH_2O atoms (1.914(7)–1.968(7) Å). The lithium tetrahedra are connected with one another by the H bonds of H_2O molecules (Figure S15), forming layers parallel to the (100) plane. Between the layers are the stacks of L^\bullet radical anions, and inside the stacks the shortest $\text{C}\cdots\text{O}$ distances are 3.123(4) Å. The angles at the pyrazine N_P atoms are the same and equal to $109.9(3)^\circ$. The geometrical parameters of $[\text{L}]$ in the lithium salt are listed in Table S8.

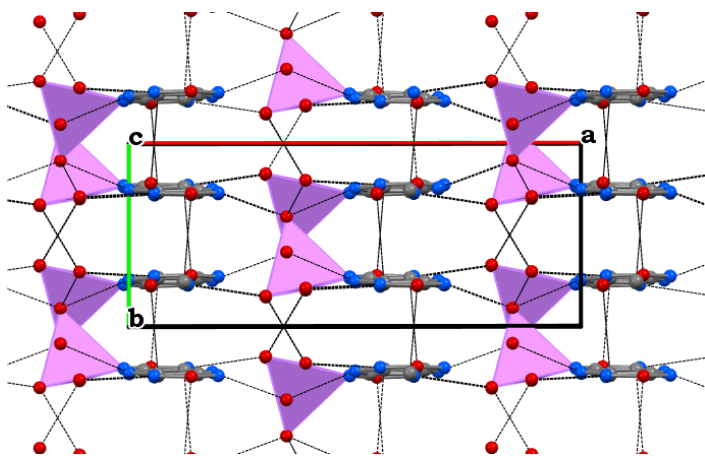


Figure S15. Fragment of the structure of $[\text{Li}(\text{L}^\bullet)(\text{H}_2\text{O})_3]$.

The salt $\text{Na}(\text{L}^\bullet)(\text{H}_2\text{O})_3$ differs in symmetry, although it has a similar composition as $\text{Li}(\text{L}^\bullet)(\text{H}_2\text{O})_3$. The columns of $\text{O}\cdots\text{O}$ edge-sharing Na octahedra (the equatorial $\text{Na}-\text{OH}_2\text{O}$ distances are 2.409(2)–2.424(2) Å, and the axial $\text{Na}-\text{N}$ distances are 2.523(2) Å) are linked into layers by L^\bullet radical anions (Figure S16). The crystallization H_2O molecules connect the layers into a framework. The distances and bond angles in the two crystallographically independent L^\bullet radical anions are close. Note that the $\text{C}-\text{N}_\text{P}$ distances in the pyrazine rings are slightly different ($\text{C3}-\text{N4}$ 1.381(3)–1.382(3), $\text{N4}-\text{C5}$ 1.395(3)–1.396(3) Å), the angles being the same: $109.2(2)$ – $109.2(2)^\circ$ (Table S8).

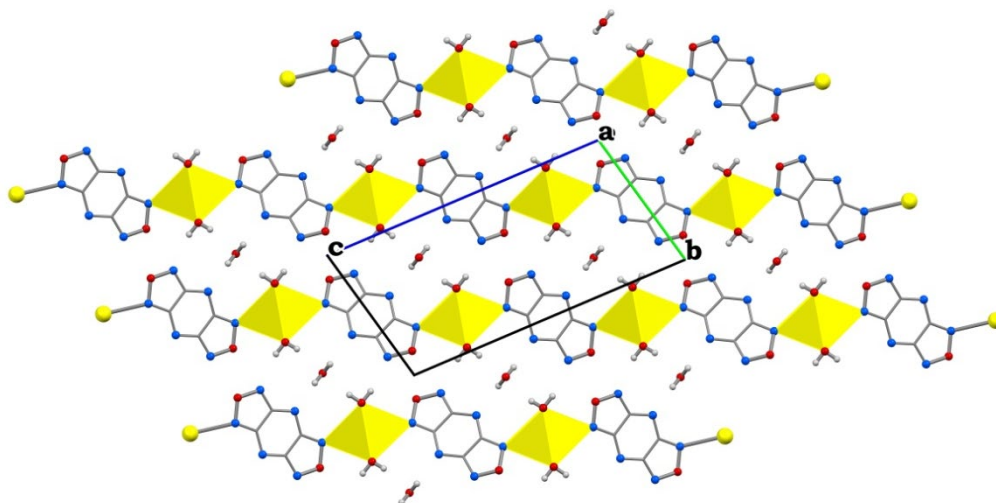


Figure S16. Fragment of framework in the structure of $\text{Na}(\text{L}^*)(\text{H}_2\text{O})_3$.

Table S8. Bond lengths and angles (Å, deg) at N_F atoms in the Li, Na, and K salts. The atomic numbering in L^* is shown in Scheme S2.

Parameter	Li(L [•])(H ₂ O) ₃	Na(L [•])(H ₂ O) ₃		K(L [•])(H ₂ O) _{2.5}	Rb(L [•])(H ₂ O)	
M-N	1.914(7)–	2.523(2), 2.532(2)		2.702(1)–	2.833(6)–	
	2.831(1)			3.506(6)		
	2.977(1)–					
M-O	2.209(8)	2.410(2), 2.409(2), 2.421(2), 2.424(2)		2.982(1),	3.057(6)–	
				3.203(1),	3.627(2)	
				3.449(1)		
O1-N2	1.390(4)	1.395(3)	1.396(3)	1.387(2)	1.384(9)	1.407(10)
N2-C3	1.321(5)	1.325(3)	1.323(3)	1.323(2)	1.318(11)	1.322(9)
C3-N4	1.337(5)	1.351(3)	1.347(3)	1.349(2)	1.311(11)	1.329(9)
N4-C5	1.350(5)	1.347(3)	1.348(3)	1.349(2)	1.390(9)	1.381(10)
C5-N6	1.320(5)	1.325(3)	1.326(3)	1.319(2)	1.304(9)	1.300(10)
N6-O7	1.388(5)	1.381(3)	1.382(3)	1.387(2)	1.369(10)	1.427(9)
O7-N8	1.384(5)	1.395(3)	1.396(3)	1.390(2)	1.386(9)	1.397(11)
N8-C9	1.317(5)	1.325(3)	1.323(3)	1.325(2)	1.312(11)	1.329(10)
C9-N10	1.342(5)	1.351(3)	1.347(3)	1.343(2)	1.319(10)	1.318(9)
N10-C11	1.337(4)	1.347(3)	1.348(3)	1.355(2)	1.394(9)	1.364(9)
C11-N12	1.318(5)	1.325(3)	1.326(3)	1.315(2)	1.310(10)	1.312(10)
N12-O1	1.392(4)	1.381(3)	1.382(3)	1.395(2)	1.386(10)	1.415(9)
C3-C11	1.463(5)	1.446(3)	1.451(3)	1.447(2)	1.500(10)	1.406(10)
C5-C9	1.457(5)	1.446(3)	1.451(3)	1.445(2)	1.501(10)	1.406(10)
∠C3-N4-C5	109.9(3)	109.2(2)	109.3(2)	109.7(1)	112.1(7)	107.4(6)
∠C9-N10-C11	109.9(3)	109.2(2)	109.3(2)	109.6(1)	112.3(7)	107.3(7)

In the structure of $\text{K}(\text{L}^*)(\text{H}_2\text{O})_{2.5}$, the polyhedra of K atoms are formed by four $\text{O}_{\text{H}_2\text{O}}$ atoms and two N_F atoms of the furazan rings of two L^* radical anions with the distances $\text{K-O} = 2.702(1)\text{--}2.831(1)$ Å and $\text{K-N} = 2.977(1)\text{--}2.982(1)$ Å. The $\text{O}\cdots\text{O}$ edge-sharing polyhedra form columns

along [010], which are linked into double layers by the $L^{\bullet-}$ radical anions (Figure S17). The water molecules lying between layers are H-bonded with them, forming a framework. The distances and bond angles in $L^{\bullet-}$ are close to those in $Na(L^{\bullet-})(H_2O)_3$ (Table S8).

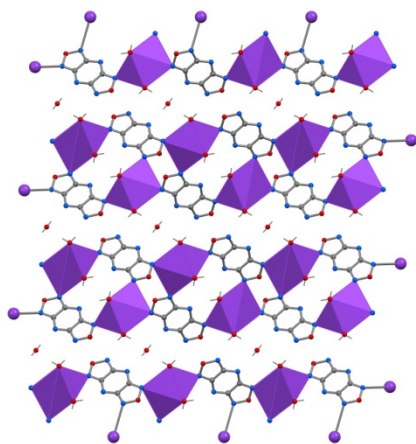


Figure S17. Fragment of the structure of $K(L^{\bullet-})(H_2O)_{2.5}$ projected along the [010] direction.

For rubidium, dark green crystals of $Rb(L^{\bullet-})(H_2O)$ were obtained. In the structure of $Rb(L^{\bullet-})(H_2O)$, the twin columns of Rb octahedra linked by ligands form a framework (Figure S18). The Rb–O and Rb–N distances are in the range 2.833(6)–3.342(8) Å; the bond lengths in the two crystallographically independent $L^{\bullet-}$ radical anions are close (Table S8), while the CNC angles in the pyrazine rings differ significantly: 112.2(7) and 107.3(7)°. In this structure, we encounter for the first time the metal atom bonded not only with the furazan N_F atoms, but also with the pyrazine N_P atoms, the Rb– N_P distances (3.056(6)–3.078(7) Å) being shorter than the Rb– N_F ones (3.057(6)–3.290(7) Å). Note that the distances to the O_F atoms (3.326(7) and 3.369(6) Å) are only slightly longer than the maximum Rb– N_F distance of 3.290(7) Å.

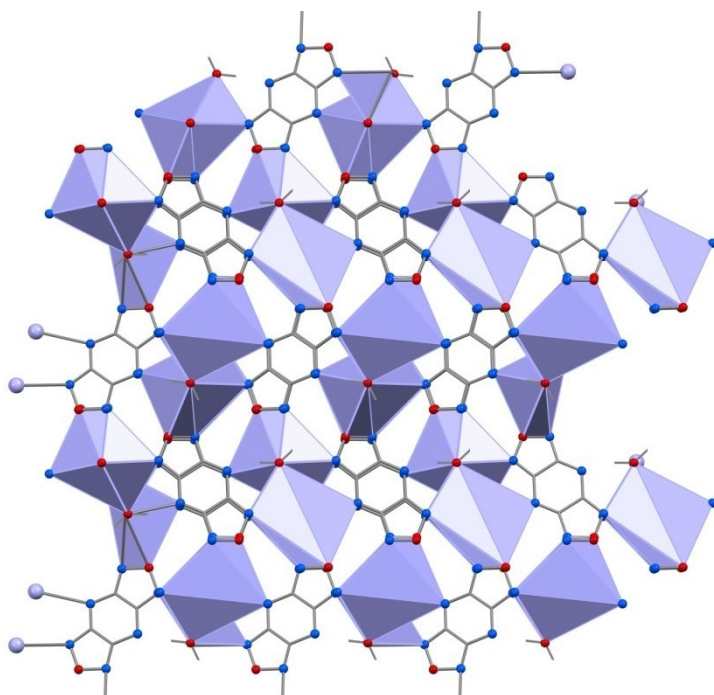
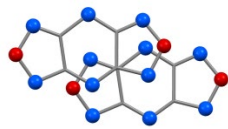
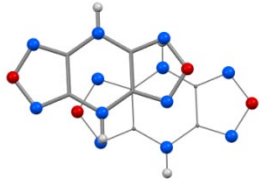


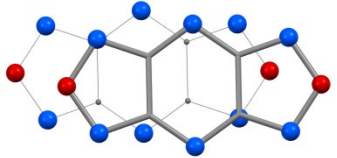
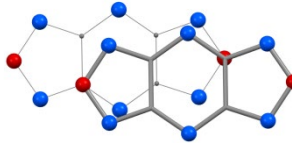
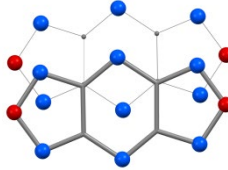


Figure S18. Fragment of framework in the structure of $\text{Rb}(\text{L}^*)(\text{H}_2\text{O})$; view along $[100]$.

As mentioned above, in the crystals of all compounds under study except L^* , difuranopyrazines form stacks similar to those described for $\text{H}_2\text{L} \cdot 2\text{DMF}$ with intermolecular distances of 3.12–3.30 Å. The mutual arrangement of molecules in stacks and the short contacts between the L atoms are shown in Table S9.

Table S9. The shortest contacts between L's in stacks.

Compound	Arrangement of neighboring molecules L	Shortest contact, Å
H_2L		C...C 3.123
$\text{H}_2\text{L} \cdot 2\text{DMF}$		C...C 3.299
$(\text{NH}_4)(\text{L}^*)(\text{H}_2\text{O})_3$		C...O 3.265
$\text{Li}(\text{L}^*)(\text{H}_2\text{O})_3$		C...O 3.123
$\text{Na}(\text{L}^*)(\text{H}_2\text{O})_3$		C...N 3.325
$\text{K}(\text{L}^*)(\text{H}_2\text{O})_{2.5}$		C...O 3.274
$[\text{Rb}(\text{L}^*)(\text{H}_2\text{O})]$		C...C 3.168

4. Magnetic properties

The magnetic susceptibility of the polycrystalline samples was measured with a Quantum Design MPMSXL SQUID magnetometer in the temperature range 2-300 K with magnetic field of up to 5 kOe. Diamagnetic corrections were made using the Pascal constants. The effective magnetic moment was calculated as $\mu_{\text{eff}}(T) = [(3k/N_A\mu_B^2)\chi T]^{1/2} \approx (8\chi T)^{1/2}$. Analysis of the experimental data was performed using PHI program.⁸

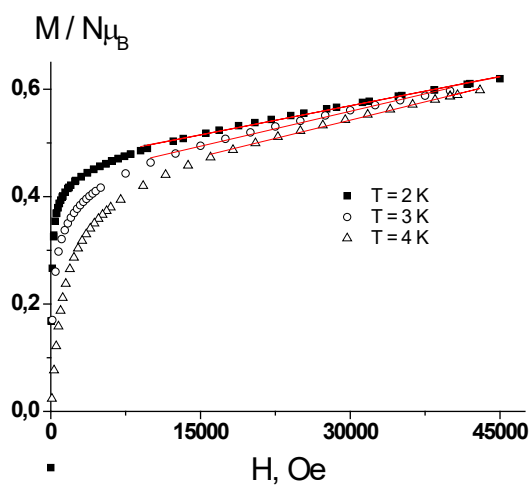


Figure S19. Dependence of M on H for $\text{Na}(\text{L}^\bullet)(\text{H}_2\text{O})_3$ at low temperatures.

The field dependences of magnetization for $\text{Na}(\text{L}^\bullet)(\text{H}_2\text{O})_3$ at 2, 3, and 4 K are presented in Figure S19. Their analysis using the equation $M = M_0 + \chi \cdot H$ allowed to evaluate the spontaneous magnetization M_0 and magnetic susceptibility χ ; the optimum values of the parameters are shown in Table S10. The M_0 values are below the theoretical value of saturation magnetization of $1 \mu_B$, which corresponds to a transition to the magnetically ordered state of approximately half of all paramagnetic centers.

Table S10. Spontaneous magnetization M_0 , magnetic susceptibility χ , and μ_{eff} for $\text{Na}(\text{L}^\bullet)(\text{H}_2\text{O})_3$ at 2, 3, and 4 K.

T, K	$M/N\mu_B$	χ , $\text{G} \cdot \text{cm}^3/\text{mol}$	μ_{eff} , μ_B
2	0.460	0.0203	0.57
3	0.429	0.0242	0.77
4	0.406	0.0253	0.90

5. Simultaneous electrochemical and electron spin resonance experiments and DFT calculation of HFC constants

The ESR experiments were performed using a Bruker EMX spectrometer equipped with an ER4102ST rectangular cavity and two-electrode convex Pt–Pt electrolytic cell controlled by a Zahner IM-6 potentiostat. The method for the preparation of solutions is similar to that described for cyclic voltammetry. All quantum-chemical calculations in the ESR field were performed using the ORCA ^[9] ver. 4.2.1 density functional in a triple-zeta basis set with two polarization functions def2-TZVPP ^[10], and an atom-pairwise dispersion correction with the Becke–Johnson damping scheme (D3BJ) ^[11] was included in all calculations. The Grid5 integration grids and TightSCF convergence criteria were applied throughout. RI-J and “chain of spheres” COSX approximation ^[12] with the def2-TZVPP/J auxiliary basis set ^[13] was used to speed up the calculations. Full geometry optimization with TightOpt convergence criteria was carried out to find the stationary points on the potential energy surfaces. Numerical harmonic frequency calculations were used to obtain the thermodynamic quantities and verify that all the stationary points found are local minima. The single-point relativistic calculations were performed using the scalar relativistic Douglas–Kroll–Hess Hamiltonian of the second order. Grid6 were also added to the calculation scheme described above.

6. Calculations

Note that DFT calculations were performed in two versions: periodic calculations of unit cell energies of spin-polarized states and molecular calculations of isolated molecules with surrounding water molecules. In the first case, the Quantum ESPRESSO 6.4 package ^[14] was employed with the conventional PBE exchange correlation functional and projector-augmented wave pseudopotentials of type X.pbe-n-kjpaw_psl.1.0.0.UPF (X is the symbol of a chemical element) from the standard PSLibrary of Quantum ESPRESSO.¹⁵ The cutoff energies of plane wave expansions were taken to be 50 Ry and 400 Ry for electronic wave functions and charge densities, respectively. In reciprocal space we used the 2×2×2 Monkhorst-Pack mesh of k-points in the first Brillouin zone. The Gaussian broadening was taken to be 0.136 eV. The Hubbard correlations on O atoms were implemented within the framework of GGA+U approximation in the Dudarev approach¹⁶ with Up(O)=5.0 eV tested previously.¹⁷ For the molecular DFT calculations of exchange integrals, the ORCA 4.2 quantum chemical package was used.¹⁸ The molecular calculations were carried out using the LC-BLYP and cam-B3LYP functionals in the def2-TZVPP basis (for the metal atoms Li, Na, K, and Rb, the corresponding def2-QZVPP basis sets were chosen). In all the cases, the pair exchange interactions were considered within the framework of the usual spin Hamiltonian $H = -2JS_{\text{R}} \cdot S_{\text{R1}}$, with exchange integrals J obtained by the traditional Broken Symmetry method.¹⁹

References

- [1]. M. D. Coburn, *J. Heterocycl. Chem.*, 1968, **5**, 83–87.
<https://doi.org/10.1002/jhet.5570050114>
- [2]. A. Gasco, G. Rua, E. Menziani, G. M. Nano, G. Tappi, *J. Heterocycl. Chem.*, 1969, **6**, 769–770. doi:10.1002/jhet.5570060532
- [3]. I. B. Starchenkov, V. G. Andrianov, *Chem. Heterocycl. Compd.*, 1997, **33**, 1219–1233 (*Khim. Geterotsikl. Soedin.*, 1997, 1402–1416). <https://doi.org/10.1007/BF02290874>
- [4]. (a) I. B. Starchenkov, V. G. Andrianov, *Chem. Heterocycl. Compd.*, 1996, **32**, 618 (*Khim. Geterotsikl. Soedin.*, 1996, 717); (b) A. B. Sheremetev, I. L. Yudin, *Mendeleev Commun.*, 1996, 247–248. doi:10.1070/MC1996v006n06ABEH000746
- [5]. G. M. Sheldrick, *Acta Crystallogr.*, 2015, **C71**, 3–8.
- [6]. I. B. Starchenkov, V. G. Andrianov, A. F. Mishnev, *Chem. Heterocycl. Compd.*, 1997, **33**, 216–228. <https://doi.org/10.1007/BF02256764>
- [7]. B. B. Averkiev, A. A. Korkyukov, M. Yu. Antipin, A. B. Sheremetev, T. V. Timofeeva, *Cryst. Growth Des.*, 2014, **21**, 5418–5427. <https://doi.org/10.1021/cg500589f>
- [8]. N. F. Chilton, R. P. Anderson, L. D. Turner, A. Soncini, and K. S. Murray, *J. Comput. Chem.*, 2013, **34**, 1164–1175, May 2013, doi: 10.1002/jcc.23234.
- [9]. F. Neese, *WIREs: Comput. Mol. Sci.*, 2012, **2**, 73–78, doi: 10.1002/wcms.81.
- [10]. F. Weigend and R. Ahlrichs, *Phys. Chem. Chem. Phys.*, 2005, **7**, 3297–3305. doi: 10.1039/B508541A
- [11]. (a) S. Grimme, J. Antony, S. Ehrlich and H. Krieg, *J. Chem. Phys.*, 2010, **132**, 154104. doi: 10.1063/1.3382344; (b) S. Grimme, S. Ehrlich and L. Goerigk, *J. Comput. Chem.*, 2011, **32**, 1456–1465. doi: 10.1002/jcc.21759
- [12]. F. Neese, F. Wennmohs, A. Hansen, U. Becker, *Chem. Phys.*, 2009, **356**, 98–109. doi: 10.1016/j.chemphys.2008.10.036
- [13]. F. Weigend, *Phys. Chem. Chem. Phys.*, 2006, **8**, 1057–1065. doi: 10.1039/B515623H.
- [14]. P. Giannozzi, S. Baroni, N. Bonini, M. Calandra, R. Car, C. Cavazzoni, D. Ceresoli, G. L. Chiarotti, M. Cococcioni, I. Dabo, A. Dal Corso, S. de Gironcoli, S. Fabris, G. Fratesi, R. Gebauer, U. Gerstmann, C. Gougoussis, A. Kokalj, M. Lazzeri, L. Martin-Samos, N. Marzari, F. Mauri, R. Mazzarello, S. Paolini, A. Pasquarello, L. Paulatto, C. Sbraccia, S. Scandolo, G. Sclauzero, A. P. Seitsonen, A. Smogunov, P. Umari and R. M. Wentzcovitch, *J. Phys. Condens. Matter*, 2009, **21**, 395502.
- [15]. A. Dal Corso, *Comput. Mater. Sci.*, 2014, **95**, 337–350.

-
- [16]. S. L. Dudarev, G. A. Botton, S. Y. Savrasov, C. J. Humphreys and A. P. Sutton, *Phys. Rev. B*, 1998, **57**, 1505–1509.
- [17]. V. A. Morozov, M. V. Petrova and N. N. Lukzen, *AIP Adv.*, 2015, **5**, 087161.
- [18]. F. Neese, *WIREs Comput. Mol. Sci.*, 8:e1327. DOI:10.1002/wcms.1327.
- [19]. M. Shoji, K. Koizumi, Y. Kitagawa, T. Kawakami, S. Yamanaka, M. Okumura and K. Yamaguchi, *Chem. Phys. Lett.*, 2006, **432**, 343–347.